Nuclear Engineering and Technology 56 (2024) 4522–4530

Contents lists available at ScienceDirect

Nuclear Engineering and Technology

journal homepage: www.elsevier.com/locate/net

Original Article

Radiological, environmental, and structural investigations of Wadi El Markh granitic rocks, southeastern desert, Egypt

Mahmoud R. Khattab [a], Waheed H. Mohamed [b], Said A. Shetaia [b,c,*], Mohamed S. Ahmed [d], Sherif A. Taalab [b,**], Diaa A. Saadawi [b], Ahmed K. Sakr [e], Mayeen Uddin Khandaker [f,g], A.Sh.M. Elshoukrofy [h], Mohamed Y. Hanfi [a,i,***]

[a] Nuclear Materials Authority (NMA), P.O. Box 530, El-Maadi, Cairo, Egypt
[b] Geology Department, Faculty of Science, Al-Azhar University, Cairo, 11884, Egypt
[c] State Key Laboratory of Estuarine and Coastal Research, East China Normal University, Shanghai, 200241, China
[d] Geology and Geophysics Department, College of Science, King Saud University, 2455, Riyadh, 11451, Saudi Arabia
[e] Department of Chemistry and Biochemistry, The University of Hull, Kingston upon Hull, HU6 7RX, UK
[f] Applied Physics and Radiation Technologies Group, CCDCU, School of Engineering and Technology, Sunway University, Bandar Sunway, 47500, Selangor, Malaysia
[g] Faculty of Graduate Studies, Daffodil International University, Daffodil Smart City, Birulia, Savar, Dhaka, 1216, Bangladesh
[h] Faculty of Science, Damanhur University, Damanhur, El Beheira, Egypt
[i] Ural Federal University, Ekaterinburg, 620002, Russia

ARTICLE INFO

Keywords:
Granitic rocks
Building materials
Radiological hazards
Magnetic analysis
Pollution index

ABSTRACT

The radiological and environmental hazards of Wadi El Markh granitic rocks were investigated, and magnetic data were used to delineate the structural framework and determine the bedrock depth in the area. The result displayed that geological structures influence the occurrence of uranium mineralization in this area and are mainly associated with altered granitic formations. The activity concentrations of radioisotopes in the regions studied showed a range of values: ^{238}U varied between 345 and 1729 Bq.kg^{-1}, averaging 980 Bq.kg^{-1}; ^{232}Th ranged from 73 to 162 Bq.kg^{-1}, with an average of 120 Bq.kg^{-1}; and ^{40}K varied from 829 to 1790 Bq.kg^{-1}, average 1245 Bq.kg^{-1}. The measured concentrations of ^{238}U, ^{232}Th, and ^{40}K in the analyzed granitic rocks samples exceeded the worldwide average of 35, 45, and 412 Bq.kg^{-1}, respectively. The primary radiological risks related to these granitic rocks were associated with the gamma radiation emitted by the radioactive elements. The statistical assessment confirmed that the main contributors to the radiological risks were uranium, potassium, and associated minerals in the granitic rocks. The entire investigation region has been determined to exceed the permissible safe radiation dose rate limit of 1 mSv/year. As a result, the study determined that the granitic rocks in the surveyed area were deemed unsuitable for construction because of their elevated levels of radioactivity. The effects of pollution on the ecological system were evaluated using several ecological indices, including the Geoaccumulation index (Igeo), Contamination factor (CF), Degree of Contamination (Cd), Pollution Load Index (PLI), Potential ecological risk factor (Eri), and Potential Ecological Risk Index (RI). Based on Cd and PLI, 100 % of the samples were found to be very highly polluted to the ecological system and suggest deterioration if used. Regarding RI, the metals were arranged as Cd > As > Co > Cu > Pb > Cr > V > Zn, with considerable risk in all samples.

1. Introduction

Aeromagnetic anomalies stem from the heterogeneous distribution of physical properties within rocks, particularly variations in magnetization and density. This geophysical method is highly sensitive to the properties of rocks located near the Earth's surface, although it also provides valuable insights into subsurface conditions. Despite being more attuned to shallow geological features, aeromagnetic surveys

* Corresponding author. Geology Department, Faculty of Science, Al-Azhar University, Cairo, 11884, Egypt
** Corresponding author. Geology Department, Faculty of Science, Al-Azhar University, Cairo, 11884, Egypt
*** Corresponding author. Ural Federal University, Ekaterinburg, 620002, Russia
E-mail addresses: said_abdelhady@azhar.edu.eg (S.A. Shetaia), sheriftaalab@azhar.edu.eg (S.A. Taalab), mokhamed.khanfi@urfu.ru (M.Y. Hanfi).

https://doi.org/10.1016/j.net.2024.06.015
Received 13 April 2024; Received in revised form 5 June 2024; Accepted 11 June 2024
Available online 12 June 2024

afford researchers the opportunity to investigate variations in magnetic properties across the entirety of the Earth's crust. Most of the rocks found in the Earth's subsurface possess magnetic properties. They have induced magnetization resulting from the Earth's magnetic field and/or remaining magnetization acquired at a time in the geological past. A magnetic survey is conducted to examine the subsurface of the Earth by analyzing the changes in the Earth's magnetic field caused by the magnetic characteristics of the underlying rocks. Analyzing the magnetic anomalies allows us to understand the underlying structure of the Earth's subsurface [1,2]. The aeromagnetic survey is a fast and cost-effective method for addressing regional problems and helps identify locations that require additional exploration [3].

Before interpretation commenced, the magnetic data underwent meticulous preprocessing involving a series of analytical and interpretive methodologies. These techniques included reduction to the pole, regional and residual separation, and depth estimation methods. These procedures were implemented within the wavenumber domain using the Geosoft Oasis Montaj package [4]. The regional and residual filtering process played a crucial role in discerning subsurface structures, notably lineaments, and fractures, by isolating and highlighting anomalous features indicative of geological discontinuities. Such preprocessing steps are essential for enhancing the interpretability and reliability of the magnetic data, paving the way for more insightful geological interpretations and resource assessments [5–7]. Industrial processes, such as mining, smelting, and other related activities, frequently release elemental species and their complexes into the environment, which degrades the environment and may put the stability of the biotic ecosystem in danger [8–10]. Exploration, exploitation, processing, and transport are all steps in producing rocks and aggregates from quarries. These processes cause rock masses to disintegrate and break down and stimulate a number of ecologically harmful reactions and processes. Among the chemical species that have been released are significant and minor nutrients and potentially dangerous heavy metals [11]. Trace elements and heavy metals are naturally present in the earth's crust, and background concentrations can change because of regional variations in environmental conditions. The issue of toxic heavy metals in the air, soil, and water is a worldwide one that poses an increasing threat to the ecosystem [12]. The environment can become contaminated with heavy metals through natural and manufactured processes. The most significant natural sources come from mineral weathering, erosion, and volcanic activity, whereas the primary human sources are mineral mining and processing, industrial processes, and waste.

The levels of natural radioactivity and exposure to terrestrial gamma-ray emissions outdoors primarily depend on the types of radioactive isotopes found in the soil throughout different areas of the Earth's crust. Various factors, such as biochemical and chemical interactions, geographical and geological conditions, and the type of parent rock during soil formation influence the presence and distribution of these isotopes in the soil [52]. Generally, igneous rocks like granite tend to have higher radioactivity levels than sedimentary rocks. However, certain sedimentary rocks like shales and phosphate rocks contain relatively high levels of radioisotopes, distinguishing them from other sedimentary rocks [13,14]. Despite naturally occurring radionuclides that raise background radiation levels, granitic rocks are commonly employed as construction materials for houses worldwide. Therefore, it is essential to evaluate the potential radiological risks to human health and measure the levels of naturally occurring radioactive isotopes [15,16]. To effectively assess the environmental impact of natural radioactivity, thoroughly comprehend the concentrations and distributions of the terrestrial isotopes. Over the past few decades, significant research has been conducted on the effects of terrestrial gamma radiation on populations in various countries and the activity concentration levels in these areas [17,50,51]. The studies aim to achieve two main objectives. The first is to assess the exposure levels of the general population to natural radioactivity in the surveyed areas, which helps in understanding potential health risks. The second objective is to create a global reference dataset for monitoring future changes in environmental radioactivity due to human activities such as nuclear and industrial processes. This reference data will enable tracking and assessment of changes in radioactivity over time and their environmental impacts. Specifically, the work focuses on delineating subsurface structures and investigating the radiological and environmental characteristics of the granitic rocks in the Wadi El Markh area.

2. Materials and methods

2.1. Geological setting

Wadi El Markh area consists mainly of Precambrian igneous and metamorphic basement, unconformably overlain to the west by undeformed flat-lying Nubian Sandstone (Fig. 1). The oldest rock units are metavolcanic, then an early magmatic phase, which is represented by diorites and granodiorites, followed by a later magmatic phase of undeformed granites, felsites, and finally, a swarm of mineralized jasperoid veins and postgranitic dykes. El Eridiya plutons covers about 70 km^2. The uranium prospect is located in the southwestern part of El Eridiya pluton. It is recorded along a central shear zone associated with jasperoid veins occupying faults and fractures that strike at varying degrees between north and east. It is usually surrounded by a nearly continuous zone of highly altered rocks.

The characteristic hydrothermal alteration features are mainly represented by silicification, kaolinization, sericitization, chlorination, carbonatization, thematization, and monetization, as well as the dark grey to black dendritic patches of manganese oxides [18,19]. There is a relationship between uranium mineralization and hydrothermal alteration. Uranium mineralization is associated with the hydrothermally altered parts of Rai Elgarra granite and is localized within several shear and fractured zones filled with jasperoid veins. Siliceous veins are highly irregular in shape and vary in thickness from a few centimeters to 3 m [20].

2.2. Sampling and analytical technique

A total of 15 granite rock samples were collected, each weighing around 250 g. These samples were then transported to Cairo's Nuclear and Radiological Regulatory Authority for further analysis. Upon arrival, the samples were immediately examined in the Radiation Protection Laboratory and securely stored in appropriately labeled polyethylene bags. In order to guarantee precise analysis, the samples were subjected to a 72-h air drying procedure at a temperature of 100 °C. Each dried sample was divided into four equal parts, weighed, and then transferred into 200-ml capacity polyethylene Marinelli beakers. After being sealed, the beakers were stored for around 38 days before conducting radiometric analysis to achieve secular equilibrium. A scintillating NaI (Tl) gamma-ray analyzer, equipped with a 7.6 cm × 7.6 cm crystal, was employed to measure the concentrations of radioactive elements (^{238}U, ^{232}Th, and ^{40}K) in the granite samples. To ensure precision, a lead shield in the shape of a cylinder with dimensions of 0.157 m in diameter, 0.205 m in length, and 0.037 m in thickness was employed to safeguard the detector. The system incorporated a spectroscopy amplifier and a multi-channel analyzer for data acquisition and analysis. The devices were linked to a computer operating the SPTR-ATC software (AT-1315). Subsequently, the net counts obtained from the gamma energy photo peaks were then utilized to determine the FWHM. The gamma energy values of the radionuclides being assessed for calculation purposes are provided as follows. The quantity of ^{238}U was calculated based on the net readings under the photopeak of ^{214}Pb (351.9 keV) and the photopeak of ^{214}Bi (609.2 keV). The concentration of ^{232}Th was determined through the weighted mean value of ^{228}Ra and ^{228}Th concentrations, utilizing their decay products in an equilibrium state. The peak energies for the decay products were as follows: ^{228}Ac = 911.2 (Pγ: 26 %) and 969 keV (Pγ: 16 %), ^{208}Tl = 583.2 (Pγ: 30.5 %) and 2614.5

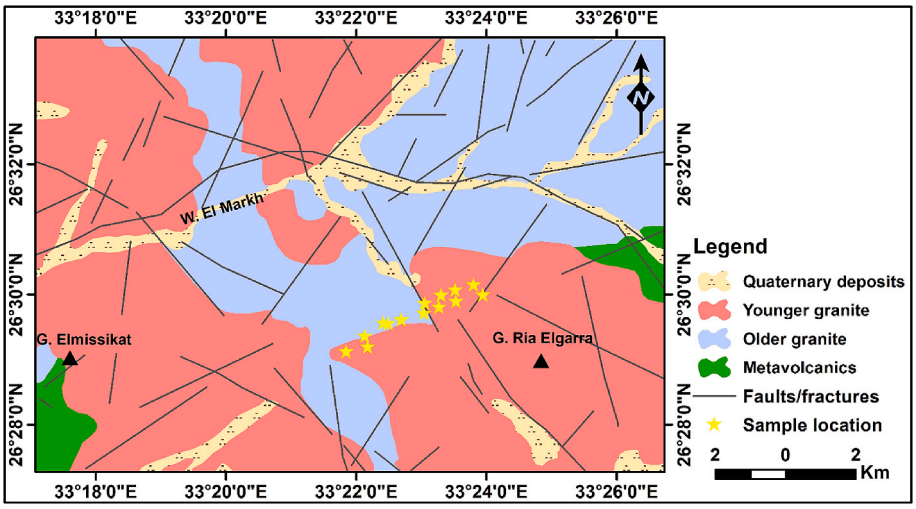

Fig. 1. Regional geologic map of the Wadi El Markh area.

keV (Pγ: 35.8 %), and ^{212}Pb = 238.6 keV (Pγ: 43.6 %). The provided measurement serves as an indication of the uranium and thorium concentration in a state of secular equilibrium with U-238, Th-232, and their respective daughter isotopes. By utilizing its 1460 keV photopeak with an abundance of 10.66 %, the activity of ^{40}K was established [21,22]. Certified standard materials, including RGU-1 for ^{238}U, RGTh-1 for ^{232}Th, and RGK-1 for 40K, are employed in quantities that are on par with those used for construction materials [23–25]. Each sample undergoes calculation to determine the minimum detection activity (MDA) for 2^{38}U, ^{232}Th, and ^{40}K, which is then adjusted based on its weight. The calculation of the minimum detectable limit (MDL) is carried out in the following manner [26]:

$$MDA = \frac{2.7 + 4.65\sqrt{B}}{M\varepsilon I_\gamma t}, \quad (1)$$

In the given equation, the variable (M) represents the mass of the sample, B denotes the background count under the peak, ε represents Efficiency of the absolute value, Iγ signifies the gamma rays's intensity, and t represents the counting time in seconds. For samples recorded up to 20000 s, the minimum detection activity (MDAs) are as follows: 2 Bq kg^{-1} for ^{238}U, 4 Bq kg^{-1} for ^{232}Th, and 12 Bq kg^{-1} for ^{40}K. The determination of radiation levels' overall uncertainty involves the utilization of the deviation equation, which takes into account both regular and stochastic misspecification. Throughout the efficiency calibration process, the radioactivity readings display systematic uncertainties varying between 0.5 and 2 percent, alongside random fluctuations of up to 5 percent [27]. The activity concentrations (Bq/kg) of each sample were calculated using the following conversions: 1%K-40, 1 ppm of U-238 and 1 ppm of Th-232 are of 313, 12.35 and 4.06 Bq kg^{-1}, respectively [28]. By analyzing the radionuclides concentrations, the radiological parameters can be computed to evaluate the dangers related to granites.

The radium equivalent content (Ra_{eq}) is a significant aspect in assessing radiation health risks. It is crucial to confirm that the Ra_{eq} value does not surpass 370 Bq kg^{-1} in order to maintain the annual effective dose (AED) for the public less 1 mSv. formula (2) for calculating Ra_{eq} can be employed based on the equilibrium condition between U-238 and Ra-226 at the detection [29]:

$$Ra_{eq}\ (Bq\ kg^{-1}) = A_{Ra} + 1.43\ A_{Th} + 0.077\ A_K \quad (2)$$

The assessment of the impact of gamma radiation emitted by radioactive sources in the atmosphere, particularly from concentrations of ^{238}U, ^{232}Th, and ^{40}K, involved the measurement of the absorbed dose rate at a distance of 1 m (Eq. (3)) [29,30].

$$D_{air}\ (nGy\ h^{-1}) = 0.430\ A_{Ra} + 0.666\ A_{Th} + 0.042\ A_K \quad (3)$$

In order to assess the levels of radioactivity, the annual effective dose (AED, mSv/y) is employed, which measures the amount of radiation exposure over the course of one year (Eq. (4)) [31].

$$AED = D_{air}\ (nGy/h) \times 0.2 \times 8760\ (h/y) \times 0.7\ (Sv/Gy) \times 10^{-6}\ (mSv/nGy) \quad (4)$$

The excess risk of cancer (ELCR) over a lifetime is a tool used to gauge the probability of fatal cancer caused by exposure to gamma radiation (Eq. (5)) [32]:

$$ELCR = AED \times DL \times RF \quad (5)$$

Where, RF is risk factor (0.05 Sv^{-1}) and DL is duration time (70 years).

The surveyed area was geophysical explored using airborne magnetic methods, with total magnetic intensity measurements conducted utilizing a high-sensitivity airborne proton-free precision magnetometer (Varian, V-85), which was installed in a tail stinger configuration. A Varian (VIW 2321 G4) single-cell cesium vapor magnetometer also served as the base station reference instrument [33]. The reduction to the pole of total intensity magnetic data can be performed automatically by utilizing the Oasis Montaj program [4]. The specific choices for analysis are the separation of regional and residual magnetic sources, upward continuation, power spectrum, source parameter image, and trend analysis techniques. In the present study, the total intensity of aeromagnetic data reduced to the pole can be calculated automatically by using the Oasis Montaj program [4] by using inclination (32.8° N), declination (1.9° E), IGRF (24425 nT), and the high of the instrument sensor from the ground surface (120 m). The reduced magnetic pole (RTP) map was separated into regional (268 m) and residual (40 m) magnetic component maps by the computed power spectrum of the magnetic data. Moreover, a series of upward continuations (to 200 m, 400 m, 600 m, 800 m, 1000 m a, and 1200 m), source parameter image, and trend analysis techniques were applied to the magnetic data.

In addition to the measurement of metal was conducted using inductively coupled plasma mass spectroscopy (ICP-MS) is an analytical technique for determining trace multi-elemental and isotopic concentrations in liquid, solid, or gaseous samples, Laboratory of Radiochemistry, Helsinki university, Finland. It combines an ion-generating argon plasma source with the sensitive detection limit of mass spectrometry detection. The digested samples were also analyzed using an Agilent 7900 ICP-QQQ with ISIS 3 loop injection system and SPS4 automatic sampler for major and trace element analysis with Mass Hunter analysis software. The elemental standard solutions were prepared by diluting a

single-element standard solution (Merck). Standard and samples were diluted with suprapure 5 % HNO3 (65 %) prior to analysis by ICP-MS.

2.3. Ecological indices

2.3.1. Geoaccumulation index (I_{geo})

The level of contamination was assessed using Muller's (1986) [34] index of proposed geographic accumulation (Igeo = Log2 (Cm/1.5 * Bn)), where C_m is the estimated metal concentration, Bn is the background value of granite [35] (Table S2), and 1.5 is for the correction of anthropogenic impacts.

2.3.2. Degree of Contamination (C_d)

Hakanson (1980) adopted the degree of contamination (Cd) as the following to assess the sum of all pollution at a specific site according to Eq. (6).

$$C_d = \sum_{i=1}^{n} CF^i = \sum_{i=1}^{n} \frac{C_m}{Bn} \tag{6}$$

CF is the contamination factor, and n is the metal count. Table S1 lists the terminologies of Cd and CF.

2.3.3. Potential Ecological Risk Index (RI)

The potential ecological risk index (RI) is frequently used to assess the total threats posed by heavy metals [36,37]. Hakanson (1980) suggested the following formula (7) to determine RI [38].

$$RI = \sum_{i=1}^{n} Er^i = \sum_{i=1}^{n} Tr^i.CF^i = \sum_{i=1}^{n} Tr^i.C_m \Big/ Bn \tag{7}$$

Whereas Tr^i denotes a metal's toxic response factor (Cr = 2, Ni = 5, Co = 5, V = 2, Cu = 5, Pb = 5, As = 10, Cd = 30 and Zn = 1), E_r^i denotes a potential ecological risk factor. Table S1 provides the RI and Er^i nomenclature.

3. Result and discussion

3.1. Magnetic data

The reduced-to-northern magnetic pole (RTP) map (Fig. 2a) reveals high magnetic anomalies in the northern and western parts of the study area, with magnetic field strengths between 42,425 nT and 42,599 nT, attributed to shallow magnetic sources and thin sedimentary covers. These high anomalies primarily follow north-south (N–S) and northwest-southeast (NW-SE) orientations. In contrast, low magnetic anomalies are found in the southeastern and western parts, associated with older granitic rocks and quaternary deposits, showing northeast-southwest (NE-SW), NW-SE, and N–S orientations. The regional magnetic map (Fig. 2b), derived by subtracting residual anomalies from total intensity anomalies, highlights high anomalies in the northern and western regions due to older and younger granitic rocks, while the southeastern and western sectors exhibit lower magnetic values and frequencies. The residual magnetic map indicates localized geological features like faults and ore bodies, with anomalies aligned along N–S and NW-SE patterns (Fig. 2c). Upward continuation analysis, performed at heights ranging from 200 m to 1200 m (Fig. S1 a,b,c, and d), shows that as continuation height increases, the influence of shallower features diminishes, helping to characterize the regional anomaly field and offering insights into subsurface structures and mineral deposits.

To estimate the depths of magnetic sources, power spectrum analysis and Source Parameter Imaging (SPI) were used. The power spectrum curve (Fig. S2a) reveals two primary levels, with mean depths for regional and residual sources calculated at 680 km and 40 m, respectively, indicating differences in source depth and the size of the magnetic anomalies (Fig. S2a). SPI analysis shows shallow magnetic sources at about 33 m beneath younger granitic rocks, while deeper sources at approximately 680 m are within older granitic regions (Fig. S2b).

Structural lineament analysis, illustrated by Rose plots, identifies deep-seated intra-basement features and near-surface geological boundaries (Fig. S3 a, b, c). The primary orientations of these lineaments are N–S, NNW, and NE-SW for regional features, and N–S, NNW-SSE, and NW-SE for shallow structures, suggesting that geological features and fault systems significantly influence the area's structural configuration.

The radioelement contour maps reveal distinct geochemical properties of the study area, highlighting the distribution of equivalent Uranium (eU), equivalent Thorium (eTh), Potassium (K), and equivalent Radium (eRa). In the northeastern region, intermediate eU concentrations (65–91 ppm (Fig. S4a),), intermediate to high eTh concentrations (31–38 ppm (Fig. S4b)), K concentrations (2.24%–3.53 id="-crosref0301"% (Fig. S4c),), and eRa concentrations (7.6–13.9 ppm (Fig. S4d),) indicate significant geochemical diversity. The northwestern quadrant also shows notable geochemical characteristics. Conversely,

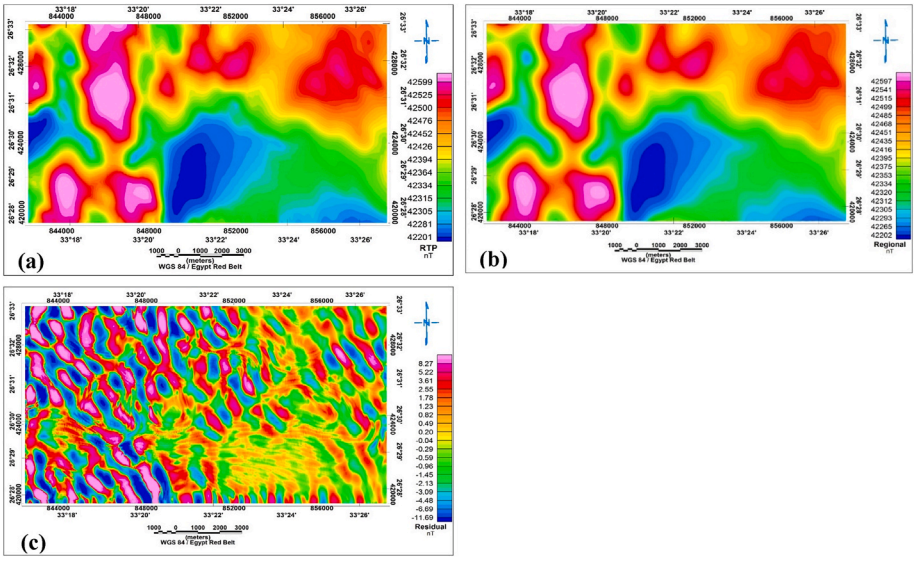

Fig. 2. (a) the reduction to the study area's northern magnetic pole (RTP) map, (b) the regional magnetic map at an average depth of 640 m, (c) the residual magnetic map, at an average depth of 40 m.

the southeastern sector, characterized by younger granite rocks of G El-Garrah, exhibits lower concentrations of these radioelements: eU (34–65 ppm (Fig S4a)), eTh (19.7–25.5 ppm (Fig. S4b),), K (2.24%–3.43 % (Fig. S4c),), and eRa (7.6–13.9 ppm (Fig. S4d),). This contrast underscores the differing geological and geochemical features between the northeastern and southeastern parts of the study area.

The ternary composite image technique uses color composites to map the concentrations of potassium (K), equivalent thorium (eTh), and equivalent uranium (eU) for geological and mineral exploration. Four distinct composite maps were analyzed: Equivalent Uranium Composite Image Map shows high uranium concentrations in older granite formations in the northwest and lower concentrations in younger granites, like Gabel El Missikat and Gabel El Garra in the northeast, indicating clear geochemical differentiation between older and younger granites (Fig. 3a). Equivalent Thorium Composite Image Map reveals high thorium concentrations in younger granite rocks at specific locations (1, 9, 10, and 11), while older granite rocks in the southwest exhibit lower thorium levels, highlighting geochemical differences between the granite formations (Fig. 3b). Equivalent Potassium Composite Image Map indicates elevated potassium levels in younger granite rocks around sample locations 14, 11, and 8, and lower levels near sample location 3, showing a distinct distribution of potassium content (Fig. 3c). Equivalent Radium Composite Image Map displays low to intermediate radium concentrations across the study area, particularly at sample locations 3, 5, and 1, suggesting consistent radium levels within this range (Fig. 3d). These maps are valuable for distinguishing zones of consistent lithology and identifying contacts between contrasting lithologies.

3.2. Assessment of radioactivity

Table 1 presents the specific activity concentrations of ^{238}U, ^{232}Th, and ^{40}K in $Bq.kg^{-1}$ alongside their uncertainties and mean values. The data illustrate noticeable fluctuations in radioactivity levels among the analyzed samples, indicating variations in geological circumstances as the likely cause [43,44]. The radioisotope activity levels in the surveyed regions ranged as follows: ^{238}U from 345 to 1729 $Bq.kg^{-1}$ (average ± SD: 980 ± 372 $Bq.kg^{-1}$), ^{232}Th from 73 to 162 $Bq.kg^{-1}$ (average ± SD: 120 ± 25 $Bq.kg^{-1}$), and ^{40}K from 829 to 1790 $Bq.kg^{-1}$ (average ± SD: 1245 ± 296 $Bq.kg^{-1}$). Notably, the radioisotope levels in the granite rock samples studied surpassed the accepted limits of 35, 45, and 412 $Bq.kg^{-1}$ for ^{238}U, ^{232}Th, and ^{40}K, respectively [45]. The elevated levels of radionuclides in the granite formations are linked to uranium and potassium-rich minerals within the granite formations in these regions, specially the samples of younger granite. Samples of granite obtained from the investigated areas displayed a variety of Ra_{eq} values ranging from 654 to 1994, averaging 1248 $Bq.kg^{-1}$. The set permissible limit stands at 370 $Bq.kg^{-1}$ [46]. All collected samples surpassed the approved threshold of 370 Bq kg^{-1} [47]. This indicates that the external radiation dose will exceed 1.5 mSv/y [45]. The efficiency of gamma radiation emitted determined the utilization of granite rocks in construction materials. Consequently, various radiological factors were calculated and are detailed in Table 1. The impact of gamma photon energy exposure on the public is evaluated through the absorbed dose rate (D_{air}) and the annual effective doses (AED). The table shows that the estimated D_{air} ranges from 298 to 922 nGy/h, with an average value of 577 nGy/h, which is higher than the UNSCEAR worldwide average of 59 nGy/h [48]. Consequently, the gamma rays emitted by the granite rocks will impact humans, leading to potential long-term health risks from exposure to gamma radiation. This can be substantiated by calculating the annual effective dose (AED) as indicated in Table 1. The average values for AED stand at 0.71 mSv/y, falling below the average's worldwide of 0.07 mSv/y as per UNSCEAR, 2010. This suggests that prolonged exposure to a low dose can have harmful health effects such as tissue damage, genetic mutations, cancer, or heart disease [49]. The minimum and maximum values for AED exceed the average's worldwide, with AED ranging from 0.37 to 1.13 mSv/y. The ELCR increased from 1.28×10^{-6} to 3.96×10^{-6} due to exposure to gamma radiation emitted by the granite rocks, with a mean value of 2.47×10^{-6}. This mean value significantly exceeds the permissible limit of $0.29 \times 10^{-6,}$ as reported by Qureshi et al., in 2014 [32]. These findings highlight the potential risk of developing cancer in the general population due to prolonged exposure to the analyzed granite rocks.

3.3. Ecological indices

According to their average values (Table S2), the metals were arranged as follows: Fe > Ba > Zn > Sr > Zr > Rb > Y > Nb > Cu > V > Pb > Hf > Co > As > Cr > Cd.

Fig. 4 illustrates the spatial distributions of metals. The estimated Geoaccumulation index (I_{geo}) fluctuates between −1.8 and 3.06. The Igeo for metals are arranged as follows based on average values: Cd > Co > Zn > As > Cu > Hf > Y > Nb > V > Cr > Pb > Ba > Zr > Rb > Fe >

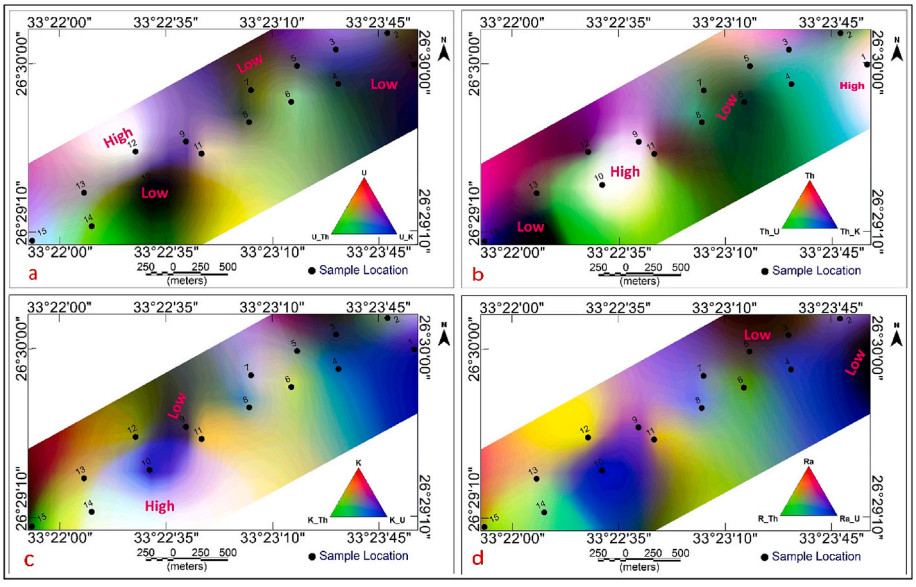

Fig. 3. Interpreted composite images of radioelements a) Equivalent uranium composite image map, b) Equivalent Thorium composite image map, c) Potassium composite image map, and d) Equivalent radium composite image map.

Table 1
Activity concentration of radionuclides (^{238}U,^{232}Th, and^{40}K) and their environmental impacts.

Samples	^{238}U	^{232}Th	^{40}K	Ra_{eq} (Bq.kg^{-1})	D_{air} (nGy.h^{-1})	AED_{out} (mSv.y^{-1})	AED_{in} (mSv.y^{-1})	ELCR × 10^{-3}
		Bq.kg^{-1}						
1	716	150	1049	1012	465	0.57	2.3	2.0
2	852	121	1155	1118	515	0.63	2.5	2.2
3	1062	133	989	1330	612	0.75	3.0	2.6
4	580	102	895	789	366	0.45	1.8	1.6
5	889	122	1230	1159	535	0.66	2.6	2.3
6	1247	85	1477	1486	688	0.84	3.4	3.0
7	988	110	1546	1273	586	0.72	2.9	2.5
8	666	106	998	897	413	0.51	2.0	1.8
9	778	158	829	1075	489	0.60	2.4	2.1
10	345	162	986	656	298	0.37	1.5	1.3
11	1642	122	1790	1958	906	1.11	4.4	3.9
12	1729	114	1327	2007	922	1.13	4.5	4.0
13	1235	118	1477	1526	702	0.86	3.4	3.0
14	1000	73	1681	1230	575	0.71	2.8	2.5
Mean	980	120	1245	1248	577	0.71	2.83	2.47
SD	372	25	296	377	176	0.22	0.86	0.75
Min	345	73	829	654	298	0.37	1.46	1.28
Max	1729	162	1790	1994	922	1.13	4.52	3.96

Sr. Spatially, 100 % of stations are classified as uncontaminated by Pb, Rb, Ba, Sr, Zr and Fe, while the majority of stations are categorized as un-moderately contaminated by Cu, Nb, Y and Hf (Fig. 5a). Moreover, the Igeo values for As and Zn indicate moderate contamination for most and all stations, respectively (Fig. 5a). Furthermore, 100 % of stations indicated moderately to heavily contaminated samples by Co. The values of Cd varied from heavily contaminated to heavily-extremely contaminated. The result of the Contamination Factor (CF) is widely extended between 0.41 and 12.50, where the metals display the following order: Cd > Co > Zn > As > Cu > Hf > Y > Nb > V > Cr > Pb > Ba > Zr > Rb > Fe > Sr. The CF values (100 %) for Rb, Ba, Sr, Zr, and Fe are lower than 1, indicating low contamination (Fig. 4b). Generally, most samples suggest moderate contamination by Cr, V, and Pb, while Nb, Y, and Hf indicated moderate contamination for all samples. Zn and As indicated considerable contamination for most samples, while Cd displayed very high contamination. The calculated degree of contamination (C_d) for the samples ranged between 39.41 and 45.39, with an average value of 42.59. Spatially, 100 % of the samples were determined to be very highly contaminated (Cd > 32) (Fig. 5c). Furthermore, the values of the Pollution Load Index (PLI) for the samples varied between 1.51 and 1.73, with an average value of 1.65. Generally, 100 % of samples have PLI >1(Fig. 5d), which suggests deteriorated samples. The computed values of the Potential Ecological Risk factor (E_r^i) for the individual heavy metals were varied between 1.65 and 3.35, 255 and 375, 32.5 and 49.5, 1.58 and 3.13, 9.9 and 15.15, 4.13 and 6.39, 31.33 and 66, 4.25 and 5.50 for Cr, Cd, Co, V, Cu, Pb, As and Zn, respectively. The average values of Eri for metals track the following order: Cd > As > Co > Cu > Pb > Zn > V > Cr. Generally, 100 % of the sample values were lower than 40 for Cr, V, Cu, Pb, and Zn, demonstrating low risk, while the values for Cd suggested high to very high risk. Regarding the calculated RI for heavy metals, the values were changed between 365.8 and 491.99, with an average value of 423.57. Spatially, 100 % of the samples were classified as considerable risk (300 ≤ RI < 600) (Fig. 5e).

4. Conclusion

Combining geophysical, geochemical, and radiometric methods in the investigation of Wadi El Markh granitic rocks in Egypt is crucial for a comprehensive understanding of the area's environmental and structural characteristics. Geophysical techniques, particularly magnetic surveys, help delineate the subsurface structures, identifying geological discontinuities and the depth of bedrock. Notably, the regional magnetic anomaly map indicates prominent magnetic trends closely correlated with a significant and extensive lineament within the area. Geochemical methods reveal the distribution and concentration of various elements, providing insights into pollution levels and ecological risks. The use of these rocks for industrial purposes like quarrying, mining, smelting, and related operations would harm the environment, according to several ecological indices, including the accumulation index, contamination factor, degree of contamination, pollution load index, potential ecological risk factor, and potential ecological risk index. Radiometric analysis highlights the radioactivity levels, crucial for assessing the potential health risks posed by natural radionuclides in construction materials. This study stands out for assessing radioactivity levels in granitic rocks, commonly used for decorative purposes and in diverse construction fields. The average activity concentrations (±SD) for ^{238}U, ^{232}Th, and ^{40}K are 980 ± 372 Bq.kg^{-1}, 120 ± 25 Bq.kg^{-1}, and 1245 ± 296 Bq.kg^{-1}, respectively, which are higher than the worldwide average values reported by UNSCEAR. In addition, a comprehensive assessment of all radiological hazard factors associated with the granitic rock samples under analysis was conducted. The finding of elevated levels above predetermined thresholds in these samples suggests that the granitic rocks under investigation include radioactive minerals such as zircon, uranophane, and uranothorite. This multidisciplinary approach ensures a detailed assessment of both the environmental impact and the suitability of the rocks for construction, ultimately revealing that the granitic rocks in the area exceed safe radiation limits and pose significant ecological and health risks due to elevated radioactivity levels and heavy metal contamination.

Data availability statement

The data supporting this study's findings are available from the corresponding author upon reasonable request.

Funding

This work is funded by the Researchers Supporting Project number (RSP2024R455), King Saud University, Riyadh, Saudi Arabia.

CRediT authorship contribution statement

Mahmoud R. Khattab: Writing – review & editing, Writing – original draft, Visualization, Validation, Supervision, Software, Resources, Project administration, Methodology, Investigation, Funding acquisition, Formal analysis, Data curation, Conceptualization. **Waheed H. Mohamed:** Writing – review & editing, Writing – original draft, Visualization, Validation, Supervision, Software, Resources, Project

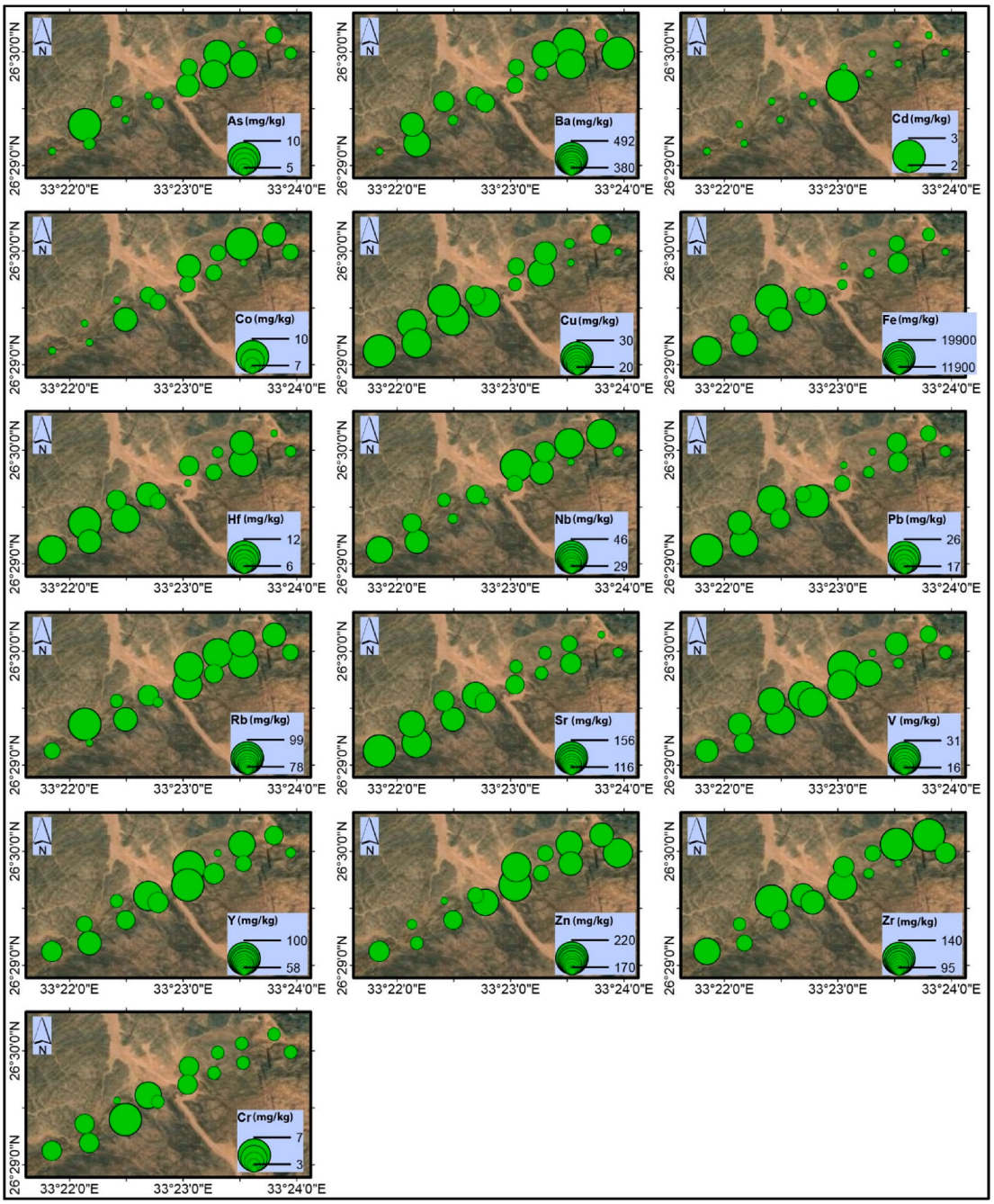

Fig. 4. Spatial distributions of elements in the study area.

administration, Methodology, Investigation, Funding acquisition, Formal analysis, Data curation, Conceptualization. **Said A. Shetaia:** Writing – review & editing, Writing – original draft, Visualization, Validation, Supervision, Software, Resources, Project administration, Methodology, Investigation, Funding acquisition, Formal analysis, Data curation, Conceptualization. **Mohamed S. Ahmed:** Writing – review & editing, Writing – original draft, Visualization, Validation, Supervision, Software, Resources, Project administration, Methodology, Investigation, Funding acquisition, Formal analysis, Data curation, Conceptualization. **Sherif A. Taalab:** Writing – review & editing, Writing – original draft, Visualization, Validation, Supervision, Software, Resources, Project administration, Methodology, Investigation, Funding acquisition, Formal analysis, Data curation, Conceptualization. **Diaa A. Saadawi:** Writing – review & editing, Writing – original draft, Visualization, Validation, Supervision, Software, Resources, Project administration, Methodology, Investigation, Funding acquisition, Formal analysis, Data curation, Conceptualization. **Ahmed K. Sakr:** Writing – review & editing, Writing – original draft, Visualization, Validation, Supervision, Software, Resources, Project administration, Methodology, Investigation, Funding acquisition, Formal analysis, Data curation, Conceptualization. **Mayeen Uddin Khandaker:** Writing – review & editing, Writing – original draft, Visualization, Validation, Supervision, Software, Resources, Project administration, Methodology, Investigation, Funding acquisition, Formal analysis, Data curation, Conceptualization. **A.Sh.M. Elshoukrofy:** Validation, Software, Resources, Data curation, Conceptualization. **Mohamed Y. Hanfi:** Writing – review & editing, Writing – original draft, Visualization, Validation, Supervision, Software, Resources, Project administration, Methodology, Investigation, Funding acquisition, Formal analysis, Data curation, Conceptualization.

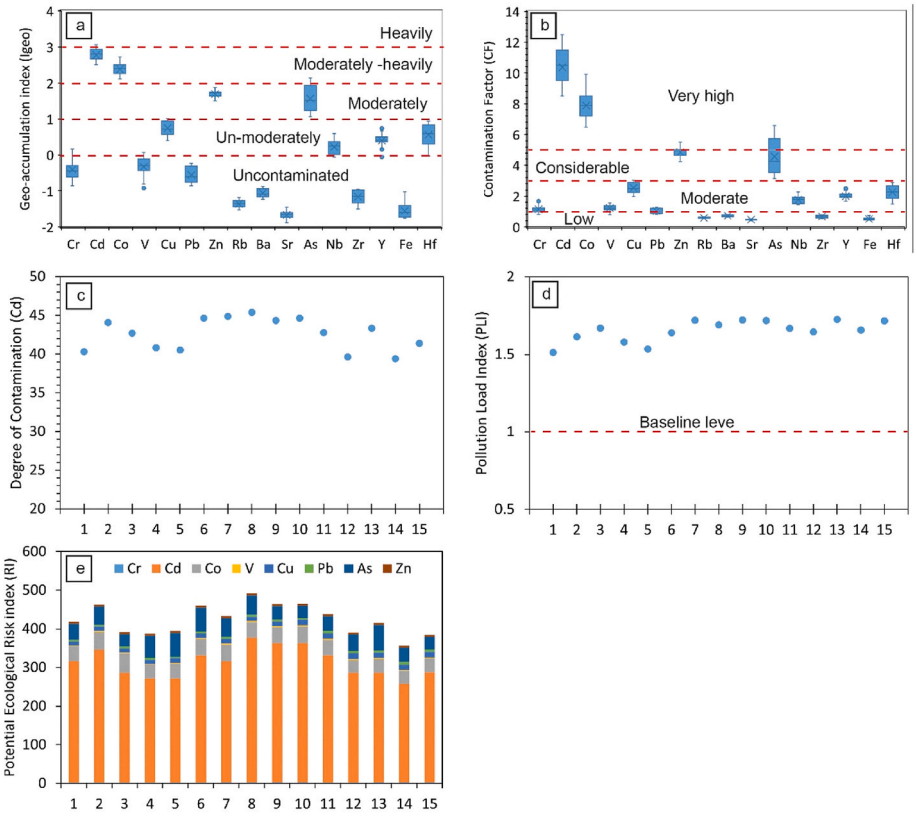

Fig. 5. a. Boxplots of accumulation index (Igeo) for elements. b. Boxplots of contamination factor (CF) for elements. c. Distribution of degree of contamination (Cd) in samples. d. Distribution of pollution load index (PLI) in samples. e. Distribution of potential ecological risk index (RI) in samples.

Declaration of competing interest

The authors declare that they have no known competing financial interests or personal relationships that could have appeared to influence the work reported in this paper.

Acknowledgments

This work is funded by the Researchers Supporting Project number (RSP2024R455), King Saud University, Riyadh, Saudi Arabia.

Appendix A. Supplementary data

Supplementary data to this article can be found online at https://doi.org/10.1016/j.net.2024.06.015.

References

[1] A. Khalil, T.H.A. Hafeez, A. El kotb, H.S. Saleh, W.H. Mohamed, E. Takla, Subsurface structural characterization as deduced from potential field data—west Beni Suef, Western Desert, Egypt, Arabian J. Geosci. 15 (2022) 1627, https://doi.org/10.1007/s12517-022-10900-1.

[2] M.M. Khalifa, W.H. Mohamed, M.A. El Ammawy, A.I. Taha, A. Awad, A.A. Orchid, Evaluation of the subsurface structural features of the Farafra Oasis, western desert, Egypt using aeromagnetic data, Model Earth Syst. Environ. 10 (2024) 723–733, https://doi.org/10.1007/s40808-023-01806-2.

[3] A. Hossain, D. Hossain, R. Abdullah, Structural and stratigraphic interpretation of geophysical data of the Fenchuganj gas field in the Surma basin, Bangladesh, J. Geol. Soc. India 86 (2015) 148–154, https://doi.org/10.1007/s12594-015-0294-4.

[4] Geosoft, Geosoft Mapping and Processing System, 2010. Toronto, Canda.

[5] I.M. Ibraheem, E.A. Elawadi, G.M. El-Qady, Structural interpretation of aeromagnetic data for the Wadi El Natrun area, northwestern desert, Egypt, J. Afr. Earth Sci. 139 (2018) 14–25, https://doi.org/10.1016/j.jafrearsci.2017.11.036.

[6] R. Abd El Rahman, S. Taalab, Z. Al Full, M. Mohamed, M. Sayyed, N. Almousa, M. Hanfi, Natural radionuclide levels and radiological hazards of khour abalea mineralized pegmatites, southeastern Desert, Egypt, Minerals 12 (2022) 353. https://doi.org/10.3390/min12030353.

[7] W.H. Mohamed, M.H. Elyaseer, M.E.M. Sabra, Structural lineament analysis of the Bir El-Qash area, Central Eastern Desert, Egypt, using integrated remote sensing and aeromagnetic data, Sci. Rep. 13 (2023) 21569, https://doi.org/10.1038/s41598-023-48660-x.

[8] A.M. El Mezayen, E.M. Ibrahim, M.G. El-Feky, S.M. Omar, A.M. El-Shabasy, S. A. Taalab, Physico-chemical conditions controlling the radionuclides mobilisation in various granitic environments, Int. J. Environ. Anal. Chem. 102 (2022) 970–986, https://doi.org/10.1080/03067319.2020.1729758.

[9] A.M. Abdel-Rahman, H.M. El-Desoky, B.N.A. Shalaby, H.A. Awad, A. Ene, M. A. Heikal, H. El-Awny, W. Fahmy, S.A. Taalab, H.M.H. Zakaly, Ultramafic rocks and their alteration products from northwestern allaqi province, southeastern desert, Egypt: petrology, mineralogy, and geochemistry, Front. Earth Sci. 10 (2022), https://doi.org/10.3389/feart.2022.894582.

[10] A.E. Omar, M.A.H. Sakr, S.A. Taalab, A.-B.A. Bakhit, M. Pugliese, G. La Verde, M. Y. Hanfi, Geotechnical and environmental radioactivity investigations at Al Sādis Min Uktōber city, Cairo municipality (Egypt), for the high-speed railway construction, Appl. Radiat. Isot. 193 (2023) 110664, https://doi.org/10.1016/j.apradiso.2023.110664.

[11] C.I. Adamu, T.N. Nganje, A. Edet, Major and trace elements pollution of sediments associated with abandoned barite mines in parts of oban massif and mamfe embayment, SE Nigeria, J. Geochem. Explor. 151 (2015) 17–33, https://doi.org/10.1016/j.gexplo.2014.12.010.

[12] S.A. Taalab, H.M.H. Zakaly, V. Ivanov, A.W. Alrowaily, H.A. Awad, N.S. Abed, S.A. M. Issa, A.M. Eltohamy, A. Ene, Notable changes in geochemical and mineralogical characteristics of different phases of episyenitization: insights on the radioactive and shielding of the late phase, Front. Earth Sci. 11 (2023), https://doi.org/10.3389/feart.2023.1241975.

[13] M. Tzortzis, H. Tsertos, S. Christofides, G. Christodoulides, Gamma-ray measurements of naturally occurring radioactive samples from Cyprus characteristic geological rocks, Radiat. Meas. 37 (2003) 221–229, https://doi.org/10.1016/S1350-4487(03)00028-3.

[14] S.A. Taalab, W.H. Mohamed, A.M. Abdel-Rahman, M.S. Alqahtani, G. La Verde, M. Pugliese, M.Y. Hanfi, F. Ambrosino, Distribution maps and hazard of radioelements from granitic rocks in an Egypt region, The European Physical Journal Plus 138 (2023) 828. https://doi.org/10.1140/epjp/s13360-023-04452-w.

[15] R. Ravisankar, J. Chandramohan, A. Chandrasekaran, J.P. Prakash, I. Vijayalakshmi, P. Vijayagopal, B. Venkatraman, Assessments of radioactivity concentration of natural radionuclides and radiological hazard indices in sediment samples from the East coast of Tamilnadu , India with statistical approach, Mar. Pollut. Bull. (2015), https://doi.org/10.1016/j.marpolbul.2015.05.058.

[16] S.A. Taalab, M. Al Meshari, Y. Alzamil, A. Abanomy, A.R. Alyahyawi, W. H. Mohamed, A. El-Taher, Radiological and ecological hazards evaluation of episyenite used as building materials, J. Radioanal. Nucl. Chem. 332 (2023) 2057–2075, https://doi.org/10.1007/s10967-023-08890-9.
[17] UNSCEAR, Exposures from natural radiation sources (annex B), sources and effects of ionizing radiation, 84–141, https://doi.org/10.1097/00004032-199907000-00007, 2000.
[18] A. Abu-Deif, M. El-Tahir, A new uranium occurrence, gabal El-Missikat prospect, central eastern desert, Egypt, J. King Abdulaziz Univ. - Earth Sci. 19 (2008) 85–97, https://doi.org/10.4197/Ear.19-1.5.
[19] M.M.F. Ghoneim, A.E.S. Abdel Gawad, VEIN-TYPE URANIUM MINERALIZATION IN THE EASTERN DESERT OF EGYPT, News of the Ural State Mining University, 2018, pp. 33–38, https://doi.org/10.21440/2307-2091-2018-1-33-38.
[20] S.I. Rabie, A.A. Abdel-Meguid, A.S. Assran, Geological and geophysical exploration for uranium mineralization in the El-Erediya prospect area, Central Eastern Desert, Egypt (1998) 169–189, https://doi.org/10.1007/978-94-011-5098-9_7.
[21] S. Arunima, R. Lekshmi, P.J. Jojo, K. Mayeen Uddin, A study on leaching of primordial radionuclides 232Th and 40K to water bodies, Radiat. Phys. Chem. 188 (2021) 109658, https://doi.org/10.1016/j.radphyschem.2021.109658.
[22] U.-K. Schkade, A. Heckel, H. Wershofen, Gamma Spectrometric Determination of the Activities of Natural Radionuclides γ-SPEKT/NATRAD, 2018.
[23] M. Iqbal, M. Tufail, S.M. Mirza, Measurement of natural radioactivity in marble found in Pakistan using a NaI(Tl) gamma-ray spectrometer, J. Environ. Radioact. 51 (2000) 255–265, https://doi.org/10.1016/S0265-931X(00)00077-1.
[24] Md.J. Abedin, Md.R. Karim, S. Hossain, N. Deb, M. Kamal, Md.H.A. Miah, M. U. Khandaker, Spatial distribution of radionuclides in agricultural soil in the vicinity of a coal-fired brick kiln, Arabian J. Geosci. 12 (2019) 236, https://doi.org/10.1007/s12517-019-4355-7.
[25] IAEA, Measurement of Radionuclides in Food and the Environment–Technical Reports, 1983. Vienna.
[26] A. Abbasi, Radiation risk assessment of coastal biota from a quasi-Fukushima hypothetical accident in the Mediterranean Sea, Mar. Pollut. Bull. 194 (2023) 115363, https://doi.org/10.1016/j.marpolbul.2023.115363.
[27] A. Papadopoulos, G. Christofides, A. Koroneos, L. Papadopoulou, C. Papastefanou, S. Stoulos, Natural radioactivity and radiation index of the major plutonic bodies in Greece, J. Environ. Radioact. 124 (2013) 227–238, https://doi.org/10.1016/j.jenvrad.2013.06.002.
[28] International Atomic Energy Agency, Nuclear fuel cycle and materials section. Guidelines for Radioelement Mapping Using Gamma Ray Spectrometry Data, International Atomic Energy Agency, 2003.
[29] M. Hasan, A. Hossain Chaity, A. Haydar, I. Ali, M. Uddin Khandaker, Elevated concentrations of terrestrial radionuclides in sand: an essential raw material used in Bangladeshi dwellings, Indoor Built Environ. 30 (2021) 1051–1061, https://doi.org/10.1177/1420326X20924835.
[30] H.K. Shuaibu, M.U. Khandaker, T. Alrefae, D.A. Bradley, Assessment of natural radioactivity and gamma-ray dose in monazite rich black Sand Beach of Penang Island, Malaysia, Mar. Pollut. Bull. 119 (2017) 423–428, https://doi.org/10.1016/j.marpolbul.2017.03.026.
[31] A. Abbasi, S.F. Mirekhtiary, Risk assessment due to various terrestrial radionuclides concentrations scenarios, Int. J. Radiat. Biol. 95 (2019) 179–185, https://doi.org/10.1080/09553002.2019.1539881.
[32] A.A. Qureshi, S. Tariq, U. Kamal, S. Manzoor, C. Calligaris, A. Waheed, ScienceDirect Evaluation of excessive lifetime cancer risk due to natural radioactivity in the rivers sediments of Northern Pakistan, J Radiat Res Appl Sci 7 (2014) 438–447, https://doi.org/10.1016/j.jrras.2014.07.008.
[33] D.T. Thompson, EULDPH: a new technique for making computer-assisted depth estimates from magnetic data, Geophysics 47 (1982) 31–37, https://doi.org/10.1190/1.1441278.
[34] Index Muller, Of geoaccumulation in sediments of the rhine river, J. Geol. 2 (1986) 108–118.
[35] S.R. Taylor, Abundance of chemical elements in the continental crust: a new table, Geochem. Cosmochim. Acta 28 (1964) 1273–1285, https://doi.org/10.1016/0016-7037(64)90129-2.
[36] E.A. Khallaf, M.M.N. Authman, A.A. Alne-na-ei, Contamination and ecological hazard assessment of heavy metals in freshwater sediments and Oreochromis niloticus (Linnaeus, 1758) fish muscles in a nile river canal in Egypt, Environ. Sci. Pollut. Control Ser. 25 (2018) 13796–13812, https://doi.org/10.1007/s11356-018-1521-5.
[37] S.A. Shetaia, A.M. Abu Khatita, N.A. Abdelhafez, I.M. Shaker, S.B. El Kafrawy, Human-induced sediment degradation of Burullus lagoon, Nile Delta, Egypt: heavy metals pollution status and potential ecological risk, Mar. Pollut. Bull. 178 (2022) 113566, https://doi.org/10.1016/j.marpolbul.2022.113566.
[38] Hakanson, An ecological risk index for aquatic pollution control, a sedimentological approach 14 (1980) 975–1001.
[43] M.A.M. Uosif, L.M. Abdel-salam, An assessment of the external radiological impact in granites and pegmatite in central eastern desert in Egypt with elevated natural radioactivity, Radiat. Protect. Dosim. 147 (2011) 467–473, https://doi.org/10.1093/rpd/ncq448.
[44] J.H. Al-Zahrani, Estimation of natural radioactivity in local and imported polished granite used as building materials in Saudi Arabia, J Radiat Res Appl Sci 10 (2017) 241–245, https://doi.org/10.1016/j.jrras.2017.05.001.
[45] UNSCEAR, Sources and Effects of Ionizing Radiation - Exposures of the Public and Workers from Various Sources of Radiation - UNSCEAR 2008 Report, 2010. New York, http://www.unscear.org/docs/reports/2008/09-86753_Report_2008_Annex_B.pdf.
[46] R.M. Amin, Gamma radiation measurements of naturally occurring radioactive samples from commercial Egyptian granites, Environ. Earth Sci. 67 (2012) 771–775, https://doi.org/10.1007/s12665-012-1538-x.
[47] C. Sabbarese, F. Ambrosino, A.D. Onofrio, V. Roca, Radiological characterization of natural building materials from the Campania region (Southern Italy), Construct. Build. Mater. (2020) 121087, https://doi.org/10.1016/j.conbuildmat.2020.121087.
[48] UNSCEAR, SOURCES and EFFECTS of IONIZING RADIATION United Nations Scientific Committee on the Effects of Atomic Radiation, 2010.
[49] USEPA, EPA Radiogenic Cancer Risk Models and Projections for the U . S . Population, 2011.
[50] N.A.M. Alsaif, M. Alotiby, M.Y. Hanfi, M.I. Sayyed, K.A. Mahmoud, B.M. Alotaibi, H.A. Alyousef, Y. Al-Hadeethi, A comprehensive study on the optical, mechanical, and radiation shielding properties of the TeO2–Li2O–GeO2 glass system, J. Mater. Sci. (2021) 15226–15241. https://doi.org/10.1007/s10854-021-06074-3.
[51] N.A.M. Alsaif, M. Alotiby, M.Y. Hanfi, K.A. Mahmoud, H.A. Al-Yousef, B. M. Alotaibi, M.I. Sayyed, Y. Al-Hadeethi, Comprehensive study of radiation shielding and mechanical features of Bi2O3-TeO2-B2O3-GeO2 glasses, J. Australian Ceram. Soc. 57 (2021) 1267–1274. https://doi.org/10.1007/s41779-021-00623-z.
[52] A.M. El Mezayen, E.K. Abu Zeid, W.S. Hosny, M.G. El-Feky, S.M. Omar, S. A. Taalab, Geochemistry, mineralogy, and radioactivity of the Abu Furad Area, Central Eastern Desert, Egypt, Acta Geochim. 38 (2019) 307–326. https://doi.org/10.1007/s11631-018-0302-7.